PHYSICAL REVIEW A **90**, 023838 (2014)

Phase dynamics in vertical-cavity surface-emitting lasers with delayed optical feedback and cross-polarized reinjection

J. Javaloyes,[1] M. Marconi,[2] and M. Giudici[2]

[1]*Departament de Fisica, Universitat de les Illes Baleares, C/ Valldemossa km 7.5, 07122 Mallorca, Spain*

[2]*Institut Non-Linéaire de Nice, Université de Nice Sophia Antipolis, CNRS UMR 7335, 06560 Valbonne, France*

(Received 6 June 2014; published 20 August 2014)

We study theoretically the nonlinear polarization dynamics of vertical-cavity surface-emitting lasers in the presence of an external cavity providing delayed optical feedback and cross-polarized reinjection. We show that, far from the laser threshold, the dynamics remains confined close to the equatorial plane of a Poincaré sphere with a fixed radius. It entails that the evolution of the system is described by two phase variables: the orientation phase of the quasilinear polarization and the optical phase of the field. We explore the complex modal structure given by the double reinjection configuration and how it evolves between the cases of single cross-polarized reinjection and single optical feedback, hence disclosing the relationship with the Lang-Kobayashi model. We also reinterpret the square-wave switching observed by J. Mulet *et al.* [Phys. Rev. A **76**, 043801 (2007)] in terms of phase kinks.

DOI: 10.1103/PhysRevA.90.023838 PACS number(s): 42.55.Px

I. INTRODUCTION

Vertical-cavity surface-emitting lasers (VCSELs) possess several advantages compared to conventional semiconductor edge-emitting lasers. The former are intrinsically single-longitudinal-mode devices, which ensures mode-hopping-free operation, and they exhibit a lower threshold with respect to the latter. The circular aperture of the VCSELs induces a high beam quality compared to the strongly astigmatic output of edge emitters, thus enabling more efficient coupling of light into optical fibers. In addition, VCSELs can be tested and operated on the wafer, thus increasing the production yield and reducing fabrication costs.

Vertical cavity lasers of large transverse dimensions may present rich spatiotemporal transverse dynamics [1–3], which can be harnessed, for instance, to create transverse localized structures [4,5]. However, such complexity can be avoided by sizing the VCSEL transverse section down to a few micrometers, thereby allowing for a single-transverse-mode emission.

On the other hand, VCSELs exhibit a nearly degenerate polarization orientation owing to their almost perfect symmetry around the cavity axis. Usually, the two polarization modes are aligned along the [1 1 0] and the [1 − 1 0] crystallographic axes, although some randomness exists due to the presence of hardly controllable strain [6]. In addition to the complex problem of the elasto-optic effects [7], the application of a voltage to the laser diode can also induce anisotropies via an electro-optic effect [8]. The existence of such favored directions is sufficient to weakly pin the polarization orientation and to define two optical modes having slightly different losses and frequencies as a result of residual anisotropies, which are termed dichroism and birefringence of the cavity.

These two polarization modes share an identical transverse spatial profile and the same carrier reservoir; thus their coupling leads to complex polarization dynamics. These devices are prone to display polarization switching [9–11] accompanied, in some cases, by polarization bistability or even by regimes where the polarization of the output oscillates in time [12]. In addition, the quasidegeneracy of the orthogonal polarization states enables efficient cross-gain modulation when the device is used as an optical amplifier.

Such peculiar properties render VCSELs promising devices for implementing useful dynamics by taking advantage of their polarization degree of freedom [13]. When VCSELs are subject to optical feedback, the polarization stability is affected, and polarization dynamics appears even in the case of perfectly isotropic feedback [14]. Polarization-rotated optical feedback, where the two linearly polarized (LP) components, LP-x and LP-y, are fed back after the LP-x component is converted into the LP-y component and vice versa, induces a regular polarization dynamics which can be as fast as ∼9 GHz [15,16]. Such symmetrical polarized cross reinjection was found to induce waveforms ranging from square waves to sinusoidal oscillations.

Asymmetrical cross-polarization reinjection (XPR), where a single polarization is fed back after being converted into the orthogonal one, was also shown to promote the occurrence of square-wave switching [17] between orthogonal polarizations with a repetition period close to twice the reinjection delay. The quasidegeneracy of the VCSEL polarization modes allows us to find rather easily this regime, which also exists in edge-emitting devices [18] for higher values of the XPR rate. A few years ago, some of us proposed to combine XPR with polarization selective optical feedback (PSF) in order to achieve passive mode locking in VCSELs [19,20]. Recently, we have also demonstrated that PSF can be used to tune and control the existence of the square-wave switching generated by XPR [21].

However, VCSELs must be described by a relatively high dimensional dynamical system that would consider the dynamics of the two polarizations as well as their interplay for the two carrier reservoirs with opposite spin orientations. In addition, the dynamics in the presence of multiple delays is known to be particularly complex [22–25], although it is known that it can have a broad range of applications, e.g., in climatology [26]. Recently, the influence of multiple delays has been studied in optics as demonstrated in the case of the double-filtered feedback configuration [27,28] or in the temporal encoding of spiral defects [29]. The VCSEL intrinsic dynamic, in addition to the presence of two different time delays, renders the analysis a formidable problem, and a reduction to a lower-dimensional system as presented, for instance, in Ref. [30] for a solitary VCSEL close to its lasing threshold would be highly beneficial.

In this paper we show that, far from the onset of laser emission, the dynamics of the VCSEL remains confined close to the equatorial plane of a Poincaré sphere with a given radius. This allows us to decouple the relaxation oscillation of the total emitted power as well as the fluctuations in the ellipticity of the emitted light from the phases dynamics of the vector state on the Poincaré sphere. We reduce the dynamical system describing the polarization evolution to a simplified one having only two phase variables: the orientation phase of the quasilinear polarization and the optical phase of the field.

We believe that such a phase model and the general methodology employed here can be useful to harness the phase and orientation dynamics of VCSEL far from threshold, which is of fundamental importance for most VCSEL applications. Indeed, such a reduction not only allows simplifying the analytical and numerical studies but may also be useful for getting insight into future applications: while optical information is usually encoded in binary levels of light intensity, next-generation communication systems will also process the phase and the polarization data. Here, the simplicity of the phase model allowed us to explore the complex modal structure given by the double-feedback configuration and also to reinterpret the square-wave switching dynamics [19,20,31] as polarization orientation kinks.

This paper is organized as follows. In Sec. II we recall the basis of our model, and we fix the order of magnitude of the parameters for which our analysis applies. Section III is devoted to the phase reduction, and we discuss the modal structure and the square-wave switching dynamics in Sec. IV. Perspective is given and conclusions are drawn in Sec. V.

II. THE MODEL

We base our theoretical analysis on the so-called spin-flip model (SFM) [32], suitably modified for incorporating the effects of PSF and XPR. We assume that the LP-y mode is fed back into itself (PSF) and cross reinjected into the LP-x mode (XPR). While the most direct way to incorporate XPR and PSF would be in terms of the linearly polarized components of the field, X and Y, the derivation of the phase model is more natural in the circular basis. The SFM model expressed in circular component reads

$$\dot{E}_\pm = (1+i\alpha)\left(G_\pm - 1\right)E_+ - zE_\mp + C_\pm, \tag{1}$$

$$T\dot{D}_\pm = 1 + P - D_\pm - G_\pm\left|E_\pm\right|^2 \mp \gamma_J\left(D_+ - D_-\right), \tag{2}$$

where $E_\pm$ are the amplitudes of the left- and right-circular components of the field and $D_\pm$ are the scaled carrier densities in the two spin channels. In Eqs. (1) and (2), time has been scaled to the cavity decay rate κ, while $T = \kappa/\gamma_e$ represents the scaled carrier lifetime and γ_J is the spin-flip carrier relaxation rate normalized to γ_e. The rate of carrier density injected into the active region above threshold is represented by P. In addition, α stands for the linewidth enhancement factor [33], and the complex parameter $z = \gamma_a + i\gamma_p$ is composed of the linear dichroism γ_a and the birefringence γ_p. We introduced the effect of ultrafast gain saturation in the expression of the gain as

$$G_\pm = D_\pm\left(1 - \frac{\varepsilon_g}{2}\left|E_\pm\right|^2\right), \tag{3}$$

with ε_g being the parameter of self-saturation. Since each component of the field interacts with only one of the two spin channels, cross saturation between E_+ and E_- does not exist. In the case where the Y component is being fed back at the complex rate $\eta\exp\left(-i\Omega\right)$ after a time τ_f and cross reinjected into the X polarization at a rate $\beta\exp\left(-ia\right)$, the expression for $C_\pm$ reads

$$C_\pm = \frac{\beta}{2i}e^{-ia}\left(E_+^{\tau_r} - E_-^{\tau_r}\right) \pm \frac{\eta}{2}e^{-i\Omega}\left(E_+^{\tau_f} - E_-^{\tau_f}\right). \tag{4}$$

A. Parameter range

The polarization-switching mechanisms in the SFM have been exhaustively analyzed in the literature [30,34]. Here, we consider the case where the VCSEL may display a large range of bistability close to threshold, and as such we consider small dichroisms and birefringences, typically of the order of a few gigahertz. To fix the ideas, we take $\gamma_p = +5.24\times10^{-2}$, which means that we denote by LP-x the reddest mode and $\gamma_a = 0$. In addition, we assume standard values for Henry's factor, $\alpha = 2$, a normalized carrier lifetime $T = 500$, and atypical normalized spin-flip rate $\gamma_s = 75$. The other values of the parameters are $\eta \sim 0.05$, $\beta \sim 0.05$, $\varepsilon_g = 0.02$, and $P = 10$, and the variance of the Gaussian white noise used in the numerical simulations is 2×10^{-2}.

The presence of two kinds of feedback with possibly dissimilar delays renders the analysis of Eqs. (1) and (2) difficult. However, far from threshold, one expects the dynamics that involve the relaxation oscillations between the total emitted power and the carrier reservoir to play only a minor role. Hence, in the following we will assume a large bias current is $P \gtrsim 10$, which typically corresponds to relaxation oscillations of the order of 10–15 GHz. In realistic experimental situations, the strong damping of the relaxations oscillations makes the laser almost a class-A system, although such definition would be meaningful only for a monomode system. Here, the standard "unsaturated" rate equations and the bare SFM do not reproduce fairly this regime of strong damping, which explains why we included in our analysis the nonlinear saturation in Eq. (3). It is worth noting that a phase reduction completely identical to the one we discuss in this paper is possible without relying on gain saturation but for unrealistic parameter ranges, i.e., $P \sim 100$, which corresponds to a device biased one hundred times above threshold. Several physical effects can contribute to the gain compression parameter ε_g, for instance, spatial hole burning in the transverse plane of the VCSEL, spectral hole burning due to saturation of the individual intraband transitions, and carrier heating. In the following, we assumed that $\varepsilon_g \in \mathbb{R}$, which is consistent with a situation dominated by spatial hole burning, i.e., interband saturation.

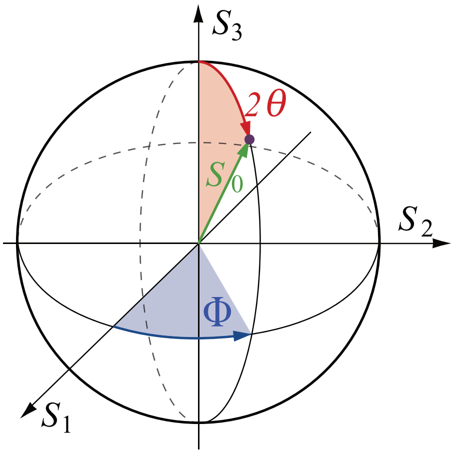

FIG. 1. (Color online) Angular representation of the VCSEL dynamics on the Poincaré sphere.

III. PHASE REDUCTION

Far from threshold, the fluctuations of the total intensity die out rapidly, and the dynamics is confined on a Poincaré sphere with a given radius. Without external perturbations, one may not expect any complex residual dynamics since the reduced dynamics is only two-dimensional. It consists of the polarization angle Φ and the ellipticity parameter θ, with the optical phase being decoupled from the rest (see Fig. 1). In addition, strongly elliptical states would incur a large energetic penalty due to the induced imbalance between the two carrier reservoirs. This further confines the residual dynamics to the vicinity of the equatorial plane, i.e., $\theta \sim \pi/4$. As such, the dynamics takes place over an invariant circle corresponding to the intersection between the equatorial plane and the Poincaré sphere.

Notwithstanding, the coherent delayed retroactions imposed by the feedback terms in Eq. (4) couple back the optical phase into the dynamics. As such, our reduced model will consist of two coupled phases, i.e., a "vectorial phase" for the orientation of the quasilinear polarization and the optical phase of the field. It is worthwhile to notice that these two phases have very different natures. While the optical phase's precise value is irrelevant due to the phase invariance in an autonomous system, the orientation phase defining the polarization direction is well fixed by the pinning imposed by the dichroism and the birefringence of the VCSEL cavity.

We now detail how the SFM with optical feedback and cross reinjection can be reduced to such a phase model far from threshold. We start by separating the modulus and phase of the circular components by defining $E_\pm = R_\pm \sqrt{2} \exp(i\psi_\pm)$, which yields, with $\Phi = \psi_+ - \psi_-$,

$$\dot{R}_+ = (N+n-1)\,R_+ - \gamma_a R_- \cos\Phi - \gamma_p R_- \sin\Phi - \varepsilon_g\,(N+n)\,R_+^3 + M_+, \tag{5}$$

$$\dot{R}_- = (N-n-1)\,R_- - \gamma_a R_+ \cos\Phi + \gamma_p R_+ \sin\Phi - \varepsilon_g\,(N-n)\,R_-^3 + M_-, \tag{6}$$

$$\dot{\psi}_+ = \alpha\,(N+n-1) + \gamma_a \frac{R_-}{R_+} \sin\Phi - \gamma_p \frac{R_-}{R_+} \cos\Phi - \alpha\varepsilon_g\,(N+n)\,R_+^2 + \frac{F_+}{R_+}, \tag{7}$$

$$\dot{\psi}_- = \alpha\,(N-n-1) - \gamma_a \frac{R_+}{R_-} \sin\Phi - \gamma_p \frac{R_+}{R_-} \cos\Phi - \alpha\varepsilon_g\,(N-n)\,R_-^2 + \frac{F_-}{R_-}, \tag{8}$$

$$T\dot{N} = 1 + P - N - (N+n)\,R_+^2 - (N-n)\,R_-^2 + \varepsilon_g[(N+n)\,R_+^4 + (N-n)\,R_-^4], \tag{9}$$

$$T\dot{n} = -\gamma_s n - (N+n)\,R_+^2 + (N-n)\,R_-^2 + \varepsilon_g[(N+n)\,R_+^4 - (N-n)\,R_-^4], \tag{10}$$

where we define the average carrier density as $N = (D_+ + D_-)/2$ and the imbalance between the two channels as $n = (D_+ - D_-)/2$, with $\gamma_s = 1 + 2\gamma_j$. The expressions for the feedback terms $M_\pm$ and $F_\pm$ are cumbersome and can be found in the Appendix. As previously mentioned, we expect the dynamics of the field to be restricted to the vicinity of the surface of the Poincaré sphere when the VCSEL is biased far from threshold. This can be evidenced by defining the sphere radius $I = (R_+^2 + R_-^2)/P$ normalized by the intensity of the solitary laser. We also introduce the ratio of the two circular components, which is a measure of the degree of ellipticity $\theta = \arctan(R_-/R_+)$; hence $R_+ = \sqrt{IP}\cos\theta$, and $R_- = \sqrt{IP}\sin\theta$. We can relate the left (right) circular components E_- (E_+) in terms of the Stokes coordinates (S_0, S_1, S_2, S_3) as described in Fig. 1 as

$$S_0 = |E_-|^2 + |E_+|^2 = 2IP, \tag{11}$$

$$S_1 = 2\mathrm{Re}(E_-^\star E_+) = S_0 \sin(2\theta)\cos\Phi, \tag{12}$$

$$S_2 = -2\mathrm{Im}(E_-^\star E_+) = S_0 \sin(2\theta)\sin\Phi, \tag{13}$$

$$S_3 = |E_-|^2 - |E_+|^2 = S_0 \cos(2\theta). \tag{14}$$

In addition we proceed to scale Eqs. (5)–(10) to the natural time scale of the relaxation oscillation frequency ω_r as $s = \omega_r t$ and define

$$\omega_r = \sqrt{\frac{2P}{T}}, \quad D = \frac{2\,(N-1)}{\omega_r}, \quad d = \frac{2n}{\omega_r}, \quad \Gamma = \frac{\omega_r}{2}(1 + P^{-1}). \tag{15}$$

With our typical values of the parameters and for bias current far from threshold, $P \sim 10$, we find that $\omega_r \sim 0.2$. In the absence of gain saturation, the relaxation oscillations are only mildly damped, as denoted by the parameter $\Gamma \sim 0.1$. In other words the laser performs approximately ten oscillations (i.e., Γ^{-1}) before reaching its steady state, in complete disagreement with any experimental evidence. This justifies the introduction of gain saturation, which strongly contributes to reducing the number of oscillations necessary to reach the equilibrium. Upon simplification of Eqs. (5)–(10)

we get

$$\begin{aligned}\frac{dI}{ds} &= DI + dI\cos(2\theta) - 2\frac{\gamma_a}{\omega_r} I \sin(2\theta)\cos\Phi \\ &\quad - 2\frac{\varepsilon_g P}{\omega_r} I^2 \mathcal{A} + \frac{\mathcal{F}}{\omega_r}, \end{aligned} \tag{16}$$

$$\begin{aligned}\frac{d\theta}{ds} &= -\frac{d}{2}\sin(2\theta) - \frac{\gamma_a}{\omega_r}\cos(2\theta)\cos\Phi + \frac{\gamma_p}{\omega_r}\sin\Phi \\ &\quad + \frac{\varepsilon_g P}{4\omega_r} I \mathcal{B} + \frac{\mathcal{G}}{\omega_r}, \end{aligned} \tag{17}$$

$$\begin{aligned}\frac{d\psi_+}{ds} &= \frac{\alpha}{2}(D+d) + \frac{\gamma_a}{\omega_r}\tan\theta\sin\Phi - \frac{\gamma_p}{\omega_r}\tan\theta\cos\Phi \\ &\quad - \alpha\frac{\varepsilon_g P}{\omega_r}\mathcal{H}_+ + \frac{F_+}{\omega_r R_+}, \end{aligned} \tag{18}$$

$$\begin{aligned}\frac{d\psi_-}{ds} &= \frac{\alpha}{2}(D-d) - \frac{\gamma_a}{\omega_r}\text{cotan}\theta\sin\Phi - \frac{\gamma_p}{\omega_r}\text{cotan}\theta\cos\Phi \\ &\quad - \alpha\frac{\varepsilon_g P}{\omega_r}\mathcal{H}_- + \frac{F_-}{\omega_r R_-}, \end{aligned} \tag{19}$$

$$\begin{aligned}\frac{dD}{ds} &= -\Gamma D - \left(1 + \frac{\omega_r D}{2}\right)(I-1) \\ &\quad - \frac{\omega_r d I}{2}\cos(2\theta) + \frac{\varepsilon_g P}{2} I^2 + \cdots, \end{aligned} \tag{20}$$

$$\frac{dd}{ds} = -\frac{\omega_r}{2} d\left(\frac{\gamma_s}{P} + I\right) - \left(1 + \frac{\omega_r}{2}D\right) I\cos(2\theta). \tag{21}$$

In Eqs. (16)–(19), we have separated the terms arising from the SFM model in the first line from the ones due to reinjections and to nonlinear gain compression in the second line. The definitions of $\mathcal{A}$,$\mathcal{B}$,$\mathcal{H}_\pm$,$\mathcal{F}$, and $\mathcal{G}$ are also given in the Appendix. In addition, we neglect several terms in the carrier equations (20) and (21) which are due to nonlinear saturation. These terms are of order $O(\varepsilon_g P \omega_r)$ and are immaterial to our analysis.

A. Parameter scaling

Equations (16)–(21) can be further simplified if one assumes the following scaling of the parameters. As a central point in our analysis, we suppose that the device operates at a large distance from threshold, e.g., $P \sim 10$. In the presence of gain saturation, this has the effect of inducing a strong damping of the relaxation oscillations. We define ε as our dimensionless smallness parameter such that $\omega_r \sim \varepsilon$, and we consider the case where η and β as well as γ_a and γ_p are of order ε^2. Typically, this corresponds to a birefringence and a dichroism of the order of ∼10 GHz, while the feedback and the cross-reinjection rates are of the order of less than a percent in reinjected power. Importantly, we assume that the gain compression coefficient ε_g is also of order ε^2, although due to the large distance from threshold, $P \sim 10$, the contribution $\varepsilon_g \omega_r^{-1} P$ is considered to be of order 1. Finally, we assume that the effective spin-flip decay term scales as $\gamma_s \sim \varepsilon^{-2}$, which corresponds to a spin-flip decay time $\gamma_J^{-1} \sim 20$ ps. Since, typically, our dimensionless smallness parameter is $\varepsilon \sim 0.2$, the errors induced by the neglect of the second-order terms in the phase model discussed in the next section are ∼4%.

B. Multiple time scales

We expand the flow around a solution defined by a quasilinear, yet undefined, polarization. In other terms we assume that there is a small ellipticity, i.e., $\theta_0 \sim \pi/4$ and $d_0 = 0$. In addition, we assume that the radius of the Poincaré sphere is close to its steady state value $I \sim I_0$, and consequently, the carriers are also around their equilibrium value $D = D_0$. In order to make apparent the scale separation between the orientation of the polarization angle and the rest of the variables, we introduce two time scales, $\sigma_0 = s$ and $\sigma_1 = \varepsilon s$, as

$$\frac{d}{ds} = \frac{\partial}{\partial\sigma_0} + \varepsilon\frac{\partial}{\partial\sigma_1}, \tag{22}$$

along with the following series expansion:

$$\begin{aligned} I &= I_0 + \varepsilon I_1(\sigma_0,\varepsilon\sigma_1) + O(\varepsilon^2), \\ \theta &= \theta_0 + \varepsilon\theta_1(\sigma_0,\varepsilon\sigma_1) + O(\varepsilon^2), \\ D &= D_0 + \varepsilon D_1(\sigma_0,\varepsilon\sigma_1) + O(\varepsilon^2), \\ d &= d_0 + \varepsilon d_1(\sigma_0,\varepsilon\sigma_1) + O(\varepsilon^2), \end{aligned} \tag{23}$$

where $\psi_\pm(\sigma_0,\varepsilon\sigma_1)$ is not expanded perturbatively. As such, the orientation $\Phi = \psi_+ - \psi_-$ can evolve freely between 0 and 2π. At zeroth order, we get the following system:

$$\frac{\partial I_0}{\partial\sigma_0} = D_0 I_0 - \frac{\varepsilon_g P}{\omega_r} I_0^2, \quad \frac{\partial D_0}{\partial\sigma_0} = 1 - I_0, \tag{24}$$

where we notice that, for our values of the parameters, the relaxation oscillations would not be damped in the absence of the nonlinear gain saturation contribution. We find that $I_0 = 1$ and $D_0 = \varepsilon_g P \omega_r^{-1}$. Nicely, the phases $\psi_\pm$ do not depend on the fast time scale since the two zeroth-order contributions cancel each other, i.e.,

$$\frac{\partial\psi_\pm}{\partial\sigma_0} = 0. \tag{25}$$

The first-order problem on the fast time scale σ_0 reads

$$\frac{\partial I_1}{\partial\sigma_0} = -D_0 I_1 + D_1 - 2\frac{\gamma_a}{\omega_r}\cos\Phi - \frac{\varepsilon_g P}{2} D_0 + \frac{\mathcal{F}_0}{\omega_r}, \tag{26}$$

$$\frac{\partial\theta_1}{\partial\sigma_0} = -\frac{d_1}{2} - \frac{\gamma_a}{\omega_r}\cos\Phi + \frac{\gamma_p}{\omega_r}\sin\Phi - \frac{\varepsilon_g P}{\omega_r}\theta_1 + \frac{\mathcal{G}_0}{\omega_r}, \tag{27}$$

$$\frac{\partial D_1}{\partial\sigma_0} = -\Gamma D_0 - I_1 + \frac{\varepsilon_g P}{2}, \tag{28}$$

$$\frac{\partial d_1}{\partial\sigma_0} = -\frac{\omega_r}{2}\frac{\gamma_s}{P} d_1 + 2\theta_1. \tag{29}$$

We notice that Eqs. (26) and (28) and Eqs. (27) and (29) correspond to two decoupled damped oscillators. While ellipticity oscillations between d_1 and θ_1 in Eqs. (27) and (29) are strongly damped with a rate $\omega_r \gamma_s P^{-1}$, the total intensity I_1 and the carrier density D_1 in Eqs. (26) and (28) oscillate and are damped only because of nonlinear gain saturation. This effect is actually hidden by the fact that $D_0 \sim \varepsilon_g \neq 0$. These two oscillators are forced by the feedback terms $\mathcal{F}_0$ and $\mathcal{G}_0$, with these terms being evaluated at zeroth order since they are proportional to η and β and therefore are already first-order quantities. At this order in the expansion, these terms depend only the slow time scale σ_1 through their dependence on variables $\psi_\pm$. We can therefore readily solve Eqs. (26)–(28) at steady state and inject the adiabatic result in the first-order problem for $\psi_\pm$ at the slow time σ_1, which reduces to

$$\begin{aligned}\frac{d\psi_+}{d\sigma_0} &= \frac{\alpha}{2}(D_1+d_1)+\gamma_a\tan\theta\sin\Phi-\gamma_p\tan\theta\cos\Phi\\ &\quad -\alpha\frac{\varepsilon_g P}{4}D_0-\alpha\frac{D_0}{2}I_1+\alpha\frac{\varepsilon_g P}{\omega_r}\theta_1+\frac{F^0_+}{\omega_r}, \qquad (30)\\ \frac{d\psi_-}{d\sigma_0} &= \frac{\alpha}{2}(D_1-d_1)-\gamma_a\text{cotan}\theta\sin\Phi-\gamma_p\text{cotan}\theta\cos\Phi\\ &\quad -\alpha\frac{\varepsilon_g P}{4}D_0-\alpha\frac{D_0}{2}I_1-\alpha\frac{\varepsilon_g P}{\omega_r}\theta_1+\frac{F^0_-}{\omega_r}. \qquad (31)\end{aligned}$$

C. Vectorial phase model

Upon replacing D_1 and d_1 from the steady-state expression of Eqs. (26) and (28), several contributions due to nonlinear saturation ε_g cancel each other, leaving only the dichroism, the birefringence, and the feedback terms to drive the motion of $\psi_\pm$. After defining $u=\arctan(\alpha)$ and $\zeta=\arctan 2(\gamma_p,\gamma_a)$, we obtain the phase model for ψ_+ and ψ_-, which reads, with $|z|=\sqrt{\gamma_a^2+\gamma_p^2}$,

$$\begin{aligned}\frac{\dot\psi_\pm}{\sqrt{1+\alpha^2}} &= |z|\sin(u\pm\psi_+\mp\psi_--\zeta)\\ &\quad+\frac{\beta}{2}[-\cos(\psi_+^{\tau_r}-\psi_\pm-a-u)\\ &\quad+\cos(\psi_-^{\tau_r}-\psi_\pm-a-u)]\\ &\quad\pm\frac{\eta}{2}[\sin(\psi_+^{\tau_f}-\psi_\pm-\Omega-u)\\ &\quad-\sin(\psi_-^{\tau_f}-\psi_\pm-\Omega-u)], \qquad (32)\end{aligned}$$

where we reintroduced the original time scale in Eq. (32) to clarify that the characteristic time scale is governed by the amplitude of the terms γ_a,γ_p,η, and β. Nevertheless, the dynamics does not necessarily need to be restricted to a particularly slow time scale; in fact, our analysis holds when the four aforementioned parameters remain smaller than the damping of the relaxation oscillations, which is typically 10–15 GHz. Hence multigigahertz dynamics can still be described by our simplified approach. Finally, we stress that the assumption by which the polarization dynamics is confined to the equatorial component on the Poincaré sphere Φ does not imply that the dynamics is limited to purely linear polarization states. Indeed, we can express the ellipticity in the Stokes components θ by solving Eqs. (27) and (29) as

$$\theta(\psi_+-\psi_-)=\frac{\pi}{4}+\frac{\mathcal{G}_0-|z|\cos(\zeta+\psi_+-\psi_-)}{P\left(2\gamma_s^{-1}+\varepsilon_g\right)}, \qquad (33)$$

and, similarly, for the spin imbalance $n=2P(\theta-\frac{\pi}{4})\gamma_s^{-1}$. Equivalent yet cumbersome expressions for the intensity and total carrier variations can be obtained in the same way. From Eq. (33), it is apparent that the typical deviations of θ with respect to $\pi/4$ and the spin imbalance δn are

$$\delta\theta\sim\pm\pi/10\,,\quad n\sim\pm0.1. \qquad (34)$$

Notice that $\delta\theta=\pi/4$ would correspond to a purely circular emission state.

IV. RESULTS

The modal structure of the VCSEL submitted to PSF and XPR is more conveniently studied by defining the half sum $\Sigma=(\psi_++\psi_-)/2$ and the difference $\Phi=\psi_+-\psi_-$. In the case of a monomode solution the difference Φ fixes the orientation of the quasilinear polarization and reaches a fix point, while the half sum drifts at the frequency of the mode under consideration. After some trigonometric simplifications Eq. (32) transforms into

$$\begin{aligned}\frac{\dot\Sigma}{\sqrt{1+\alpha^2}} &= |z|\cos\Phi\sin(u-\zeta)\\ &\quad-\eta\sin\frac{\Phi^{\tau_f}}{2}\sin\frac{\Phi}{2}\sin(u+\Omega+\Sigma-\Sigma^{\tau_f})\\ &\quad-\beta\cos\frac{\Phi}{2}\sin\frac{\Phi^{\tau_r}}{2}\sin(u+a+\Sigma-\Sigma^{\tau_r}), \qquad (35)\\ \frac{\dot\Phi}{2\sqrt{1+\alpha^2}} &= |z|\sin\Phi\cos(u-\zeta)\\ &\quad+\eta\sin\frac{\Phi^{\tau_f}}{2}\cos\frac{\Phi}{2}\cos(u+\Omega+\Sigma-\Sigma^{\tau_f})\\ &\quad-\beta\sin\frac{\Phi}{2}\sin\frac{\Phi^{\tau_r}}{2}\cos(u+a+\Sigma-\Sigma^{\tau_r}). \qquad (36)\end{aligned}$$

Interestingly, the symmetry properties of Eqs. (35) and (36) are different with respect to Σ and Φ. While Eqs. (35) and (36) are phase invariant with respect to $\Sigma\rightarrow\Sigma+\Sigma_0$, this is not the case for Φ. It is an expected result since these two phases do not have the same physical meaning: Σ is an optical phase, while Φ is an orientation angle.

Monomode solutions correspond to $\Sigma=\omega t$, while Φ is a constant. Besides the values of ω and Φ we will represent the associated ellipticity θ by using Eq. (33) and exploiting the fact that the expression for $\mathcal{G}_0$ in the case of a monochromatic solution simply reads

$$\mathcal{G}_0=2\beta\sin^2\frac{\Phi}{2}\sin(\omega\tau_r+a)-\eta\sin\Phi\sin(\omega\tau_f+\Omega) \qquad (37)$$

A. Particular cases

Before studying the general case, we will discuss several known situations as particular cases in the absence of any feedback or with only PSF.

Solitary VCSEL. We first discuss the stability of the solitary VCSEL that is governed by a single equation for Φ as given by Eq. (36), which, after simplification, reads

$$\dot\Phi=2(\gamma_a+\alpha\gamma_p)\sin\Phi; \qquad (38)$$

the solutions $\Phi_x=0$ and $\Phi_y=\pi$ correspond, respectively, to a saddle and a node when $\gamma_a+\alpha\gamma_p>0$ and vice versa in the opposite case. The frequency of two such modes can be deduced from Eq. (35), which reads

$$\dot\Sigma=(\alpha\gamma_a-\gamma_p)\cos\Phi_{x,y}=\omega_{x,y}. \qquad (39)$$

The stability diagram is depicted in Fig. 2. Notice that the stability diagram of Fig. 2 is much simpler than, for instance,

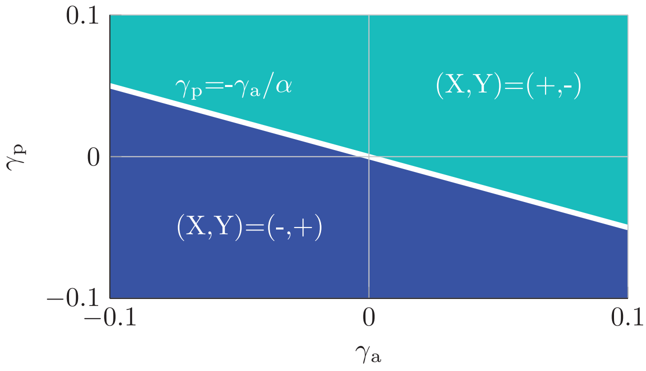

FIG. 2. (Color online) Stability diagram of the solitary VCSEL far from threshold. The condition $\gamma_a + \alpha\gamma_p = 0$ separates the two parameter regions where the stable emission is along the LP-y or the LP-x axis. Stable (unstable) emission is depicted by a minus sign (plus sign).

the analysis performed in Ref. [30], and no bistability is found in our analysis since we are in the limit of bias current values far from threshold. However, we have numerically checked the accuracy of the stability information predicted by Eq. (38), and we have found good agreement, in the sense that the condition $\gamma_a + \alpha\gamma_p = 0$ indeed separates monostable emission along LP-x from LP-y. It is worth noting that, even in the limit of bias current far from threshold, a very small region of bistability has been found in the vicinity of the line $\gamma_a + \alpha\gamma_p = 0$, represented in Fig. 2. Since our simplified model is built perturbatively upon an expansion, it is not surprising that usually negligible terms may dominate the stability in small regions of parameter space where the first-order terms vanish.

LP-x emission. Irrespective of the values of η and β, pure emission along the X axis of the solitary VCSEL is always possible since the existence of this mode is obviously not affected by optical feedback into Y and cross-polarized reinjection of Y into X. This formally corresponds to the solution $\Phi = 0$, which solves Eq. (36) while Eq. (35) reduces to the expression of the frequency of the LP-x solution at frequency $-\gamma_p$ pulled by the interplay of the dichroism γ_a and α, i.e.,

$$\omega_x = \sqrt{1+\alpha^2}\,|z|\sin(u-\zeta) = \alpha\gamma_a - \gamma_p \qquad (40)$$

where we used trigonometrical identities to simplify the last result.

LP-y Lang-Kobayashi modes. In the case where there is only optical feedback, i.e., $\beta = 0$, the solution $\Phi = \pi$ solves Eq. (36). This case corresponds to a linear polarization along the Y axis, and Eq. (35) reduces exactly to the locus of the modes of the Lang-Kobayashi model,

$$\omega_y - \gamma_p + \alpha\gamma_a + \eta\sqrt{1+\alpha^2}\sin(u+\Omega+\omega_y\tau_f) = 0, \qquad (41)$$

with the only difference being that the ellipse of the modes is shifted by the birefringence γ_p, as well by the contribution $\alpha\gamma_a$.

General equation defining the modal structure. In the general case, the presence of cross polarization makes it so that the orientation cannot perfectly align with the LP-y direction; hence $\Phi \neq 0,\pi$. This allows us to simplify Eq. (36) by dividing by $\sin\Phi$ and to express the orientation as a function of the frequency as

$$\frac{\Phi}{2} = \arctan\frac{2\,|z|\cos(u-\zeta) + \eta\cos(u+\Omega+\omega\tau_f)}{\beta\cos(u+a+\omega\tau_r)}. \qquad (42)$$

Such a value of Φ must be replaced in Eq. (35) to yield the locus of the quasilinear modes as solutions of

$$\begin{aligned}\frac{\omega}{\sqrt{1+\alpha^2}} &= |z|\cos[\Phi(\omega)]\sin(u-\zeta)\\ &\quad - \eta\sin^2\left[\frac{\Phi(\omega)}{2}\right]\sin(u+\Omega+\omega\tau_f)\\ &\quad - \beta\sin[\Phi(\omega)]\sin(u+a+\omega\tau_r). \qquad (43)\end{aligned}$$

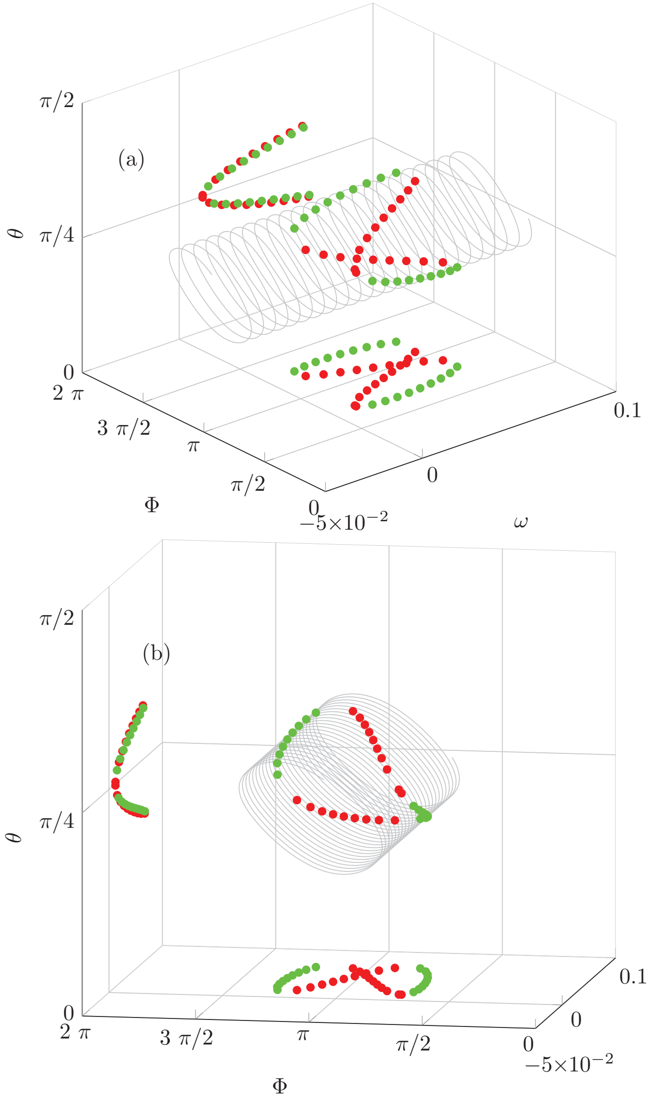

FIG. 3. (Color online) Monochromatic solutions of Eqs. (35) and (36) for $\eta = 0$, $\beta = 0.05$, and $\tau_r = 1000$. The solutions are arranged around a tube defined by the function $\Phi(\omega)$ and $\theta(\omega)$ assuming ω is a continuous variable. Stable and unstable solutions are represented in green (light gray) and red (dark gray), respectively. The number of stable and unstable solutions (S,U) is (18,19).

B. Cross-polarized reinjection only

In the case where the VCSEL is submitted to only XPR, i.e., $\eta = 0$, we recover the results obtained in Ref. [17]. It was shown in Ref. [17] that modes appear as saddle-node bifurcations for increasing values of the reinjection rate β. In addition, if the polarization selected for reinjection is the LP-y mode, the pure Y solution of the solitary VCSEL will evolve under the influence of the XPR rate, and the associated polarization orientation will rotate when β is varied. Because of the existence of this additional solution in addition to the appearance of other modes via saddle-node bifurcations, there are usually $N/2 + 1$ modes and $N/2$ antimodes. Notice, however, that in Ref. [17] the modal structure was found by solving exactly Eqs. (1) and (2) without exploiting the particular scaling of the parameters. As such, the solution was found as a determinant of a complex system of equations. Here, one is able to recognize by inspecting Eq. (43) that the locus for the modes is very similar to the one for the Lang-Koyabashi model, i.e., a transcendental equation defining the frequencies.

In addition to the solution defined by the triplet (ω,Φ,θ), we have represented (black lines in Fig. 3) $\Phi(\omega)$ and $\theta(\omega)$ as continuous functions of ω in a way similar to that in Ref. [35]; the reason for doing so will be clarified in the next section. The stability of the solutions has been analyzed using DDE-BIFTOOL [36] on Eqs. (35) and (36). Importantly, one notices in Fig. 3 that purely linear emission corresponding to solutions for which $\theta = \pi/4$ is possible. This demonstrates that cross polarization can simply rotate the direction of emission. The modal "ellipse" is centered around the frequency $\omega_y = \gamma_p - \alpha\gamma_a$ of the pure LP-y emission state, and the states closer to $\Phi = \pi$, i.e., whose polarization is closer to the LP-y mode, are the most unstable ones. In Fig. 3, which shows the external part of the projection in the (ω,Φ) plane, the stable modes are plotted in green (light gray) and correspond to the polarization orientations differing the most from the orientation of the LP-y orientation. Such modes may also present a small ellipticity. Notice that in Fig. 8 of Ref. [17], the variable n (equivalently, here θ) presented a figure-eight-shaped curve in the $(\theta|n,\omega)$ plane. Such a difference from our results is merely due to the larger values of $\beta = 0.25$ used in Ref. [17], and similar figure-eight-shaped solution curves can be found in our reduced model.

For increasing values of β more modes are created via saddle-node bifurcations, and the ellipse grows, but more and more stable modes at the exterior of the figure-eight-shaped projection become unstable up to the critical value $\beta^\star = 2\sqrt{\gamma_a^2 + \gamma_p^2}$, where all the modes are unstable (see Fig. 4). Such critical value corresponds to the onset of square-wave switching [17,18], where the two orthogonal polarizations X and Y alternate cycles of on-off emission in antiphase and at a period close to twice the delay imposed by cross-polarization reinjection τ_r. Such dynamics at twice the delay is depicted in Fig. 5.

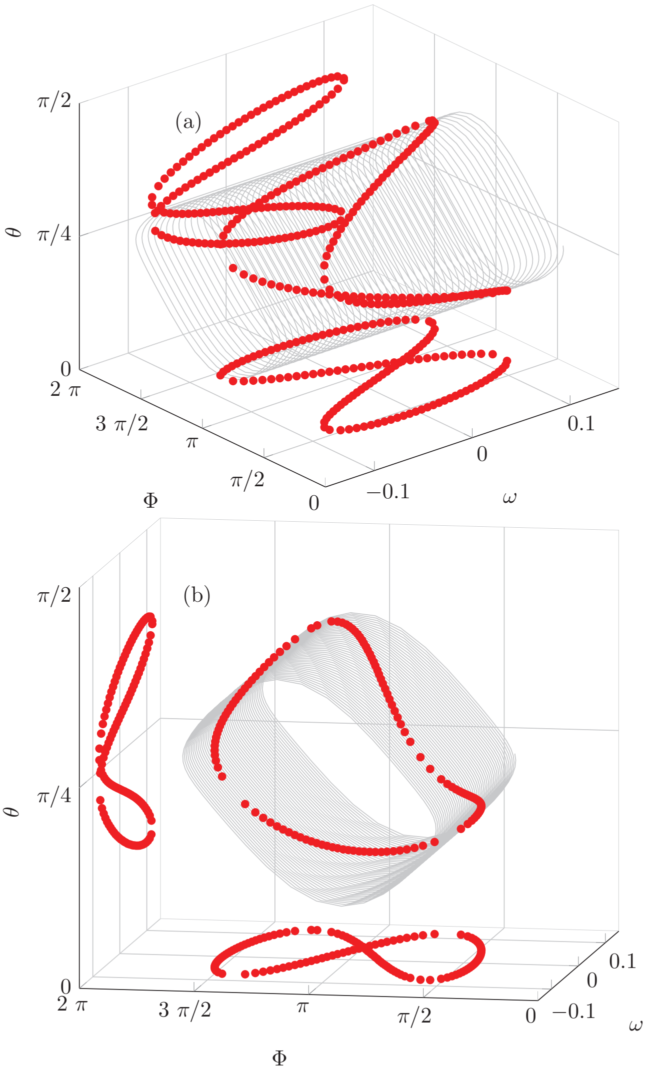

FIG. 4. (Color online) Monochromatic solutions of Eqs. (35) and (36) for $\eta = 0$, $\beta = \beta^\star + 0.01$, and $\tau_r = 1000$. There are 127 unstable solutions. Stable and unstable solutions are represented in green and red, respectively.

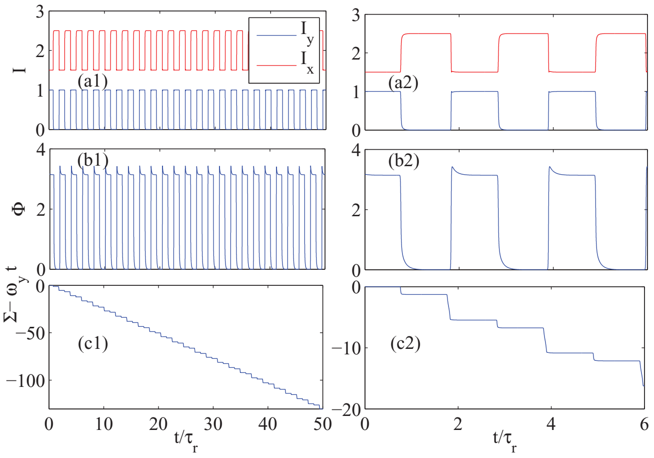

FIG. 5. (Color online) Square-wave switching as phase kinks. (a1) and (a2) The intensity of the X and Y polarization over different time scales reconstructed from the polarization orientation Φ. The traces are shifted for clarity and are actually in perfect antiphase. (b1) and (b2) The polarization orientation Φ and (c1) and (c2) the optical phase Σ from which we subtracted a drift $\omega_y t$. The parameters are $\eta = 0$, $\beta = \beta^\star + 4 \times 10^{-3}$, and $\tau_r = 1000$.

Here, we reconstruct the intensity of the X and Y components via the formulas $I_x \sim |1+e^{i\Phi}|^2$ and $I_y \sim |1-e^{i\Phi}|^2$. By construction, the antiphase relationship between the two polarizations evolutions is perfect, as one can see in Fig. 5(a1). For $\beta > \beta^\star$ we found in Figs. 5(a1) and 5(a2) a strongly nonlinear limit cycle composed of two plateaus whose period is close to twice the reinjection delay τ_r, in agreement with the results reported in Refs. [17,18,21]. Our analysis in terms of a phase-reduced model shows that it is possible to reinterpret such polarization intensity dynamics as pure phase dynamics. This is shown in Figs. 5(b1) and 5(b2), where we plot the corresponding temporal evolution of the phase Φ, which consists of kinks between π and zero and π again and can also be understood as polarization domain walls [37,38]. The evolution of the global phase Σ consists, instead, mainly of a drift at a frequency ω_y, i.e., at the frequency of the solitary VCSEL on the LP-y polarization mode. This is consistent with the fact that the first plateau corresponds

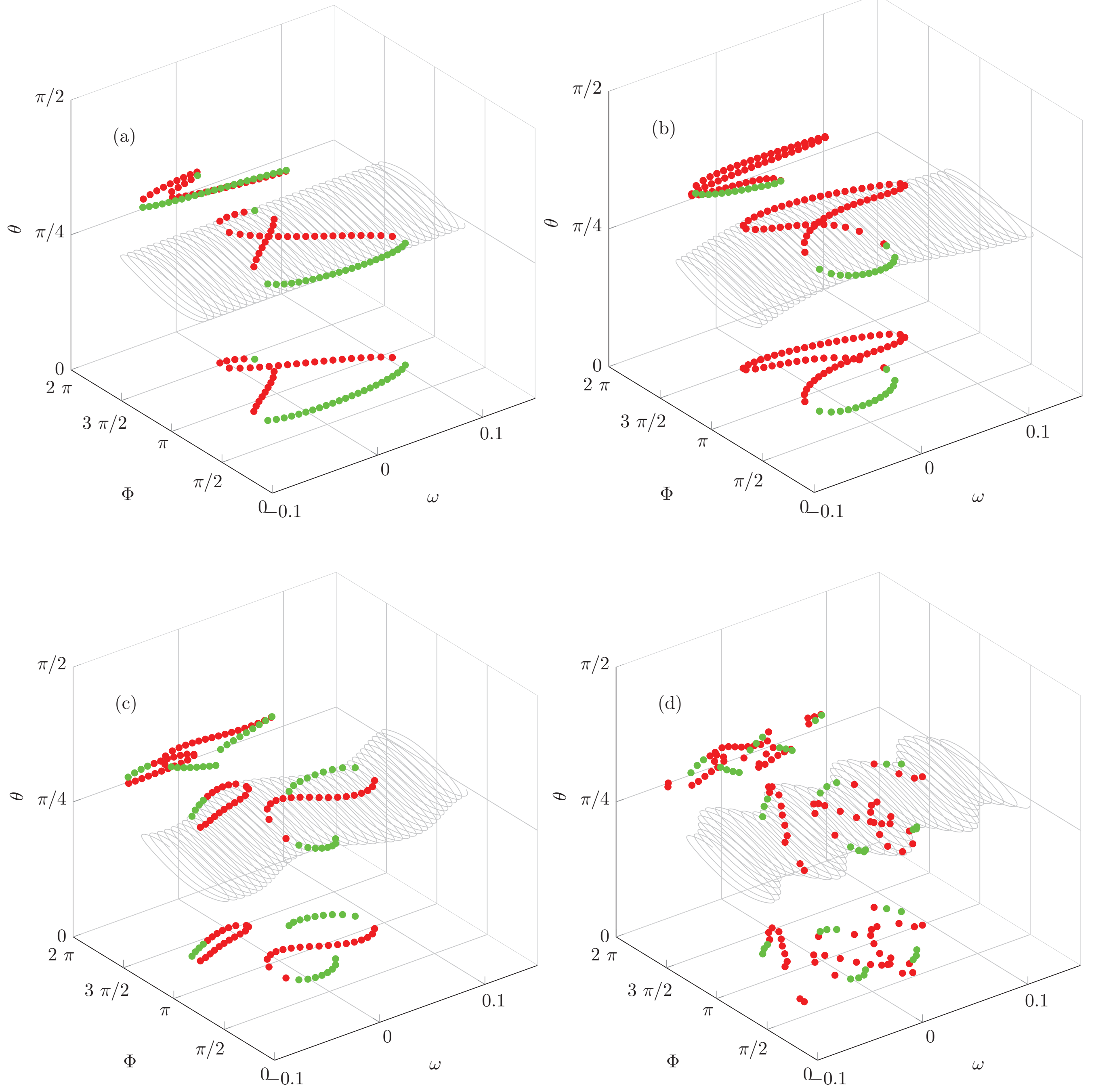

FIG. 6. (Color online) Monochromatic solutions of Eqs. (35) and (36) for $\eta = 0.025$, $\beta = 0.05$, and $\tau_r = 1000$. (a) $\Delta\tau = \tau_f - \tau_r = 0$, (b) $\Delta\tau = 20$, (c) $\Delta\tau = 40$, and (d) $\Delta\tau = 100$; the numbers of stable and unstable solutions (S,U) are (24,31), (14,55), (21,36), and (15,36), respectively.

to pure Y emission, while the second one consists of the Y mode performing injection locking into the X polarization. In both cases the frequency of emission remains locked to the frequency ω_y. Interestingly, once this drift is removed, a residual phase kink can be observed in Σ, meaning that the phase acquires a π shift at every cycle on the Poincaré sphere. However, after a rotation along the equator the polarization is actually reversed (i.e., $Y \to -Y$), and this additional phase shift of π in Σ corresponds to finding physically the exact same polarization. Such residual kinks in Σ are slaved to the square-wave switching and actually can be decoupled from the dynamics. For $\beta \gg \beta^\star$ there is excellent agreement between the full solution of Eqs. (35) and (36) and that of Eq. (36) in which we performed the substitution $\Sigma - \Sigma^{\tau_r} \to \omega_y \tau_r$, thus demonstrating that the square-wave regime can be reduced to a single equation with a delay of the type

$$\frac{d\Phi}{dt'} = \sin\frac{\Phi}{2}\left(\cos\frac{\Phi}{2} - A\sin\frac{\Phi^{\tau_r'}}{2}\right), \qquad (44)$$

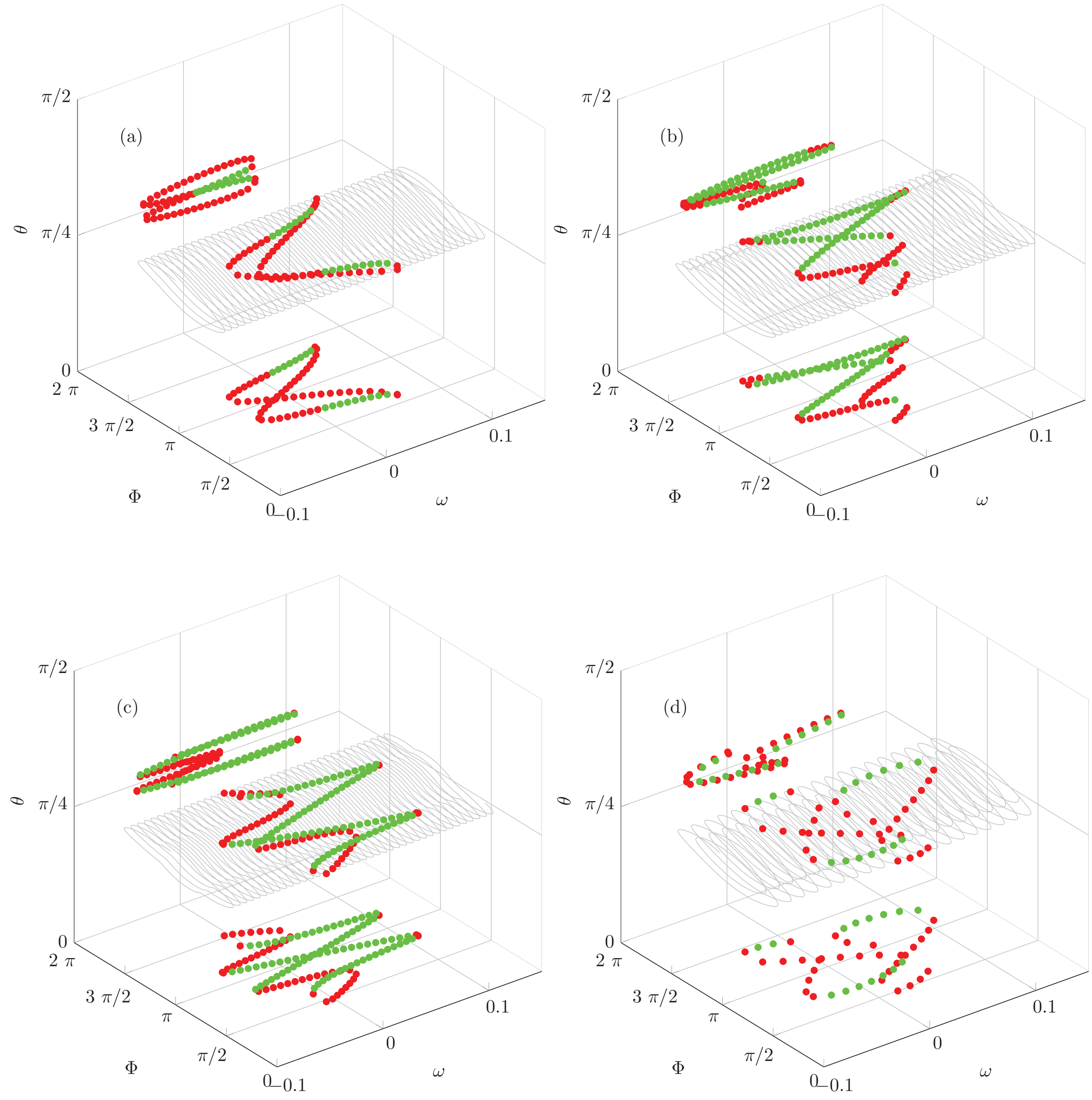

FIG. 7. (Color online) Monochromatic solutions of Eqs. (35) and (36) for $\eta = 0.025$, $\beta = 0.05$, and $\tau_r = 1000$. (a) $\tau_f = 2\tau_r$, (b) $\tau_f = 3\tau_r$, (c) $\tau_f = 4\tau_r$, and (d) $\tau_f = \tau_r/2$; the numbers of stable and unstable solutions (S,U) are (17,52), (55,36), (82,47), and (15,30), respectively.

where we have time rescaled the equation for clarity and defined an effective parameter,

$$A = \frac{\beta}{2} \frac{\sqrt{1+\alpha^2}}{\gamma_a + \alpha\gamma_p} \cos[u + a + (\gamma_p - \alpha\gamma_a)\tau_r]. \tag{45}$$

Inspection of Eq. (44) reveals that solutions composed of plateaus of duration τ_r for which either $\Phi = 0$ or $\Phi = \pi$ are indeed possible.

C. Cross polarization and feedback

In the general case where both η and β are nonzero, the modal structure depends critically on the ratio between the two delays. For small deviations from the situation $\tau_f = \tau_r$, the figure-eight-shaped modal ellipse distorts and breaks into several parts, as depicted in Fig. 6. Here, one notices that the tubular structure that supports the mode acquires a "vertical" modulation that is proportional to the ratio between the two delays. For a small mismatch between the two delays like in Figs. 6(a) and 6(b) the modal ellipse is deformed. For larger mismatches like in Fig. 5(c), the mode positions break into several subfamilies. Increasing the difference between the two delays beyond Fig. 6(d) results in a fragmented modal structure composed of quasirandomly distributed points (not shown) if observed only through a projection in the (ω,Φ) plane. We depict in Fig. 6 a bifurcation sequence for τ_f increased above τ_r, yet a similar scenario is found for $\tau_f < \tau_r$.

Once it is understood that the tubular structure oscillates at a frequency given by the ratio between the two delays, one may foresee the existence of "revivals" of relatively simple modal structures for specific ratios between the two delays. Indeed, we show in Fig. 7 that a regular structure exists whenever the feedback delay is an integer of the cross-polarization delay. Similarly, some simple structures have also been found when $\tau_f = \tau_r/n$, and we depict in Fig. 7(d) the case $\tau_f = \tau_r/2$.

D. Influence of optical feedback on the square-wave switching

As explained in Fig. 5, the second plateau of the square-wave dynamics (also described in Refs. [17,21]) results from the optical injection locking of the strong mode (say LP-y) onto the weak mode (say LP-x). At the end of the second plateau, the transitory dynamics can be understood as an escape from the vicinity of a weakly repulsive saddle where the system tries to recover the emission along the strong mode. During such an escape the system is very sensitive to noise, which induces strong period jitter in the square-wave signal. The finite time needed to perform such an escape explains why the period of the square oscillation is always slightly greater than twice the XPR delay τ_r.

The proximity of the bistable emission in parameter space as well as the existence of subtle "dynamical traps" via the folding of some unstable limit cycles induced by XPR was already described in Ref. [17] as a possible mechanism for the degradation of the square-wave signal; see Fig. 9 in Ref. [17] for more details. In the parameter region explored here (i.e., bias currents far from the threshold value) the system does not exhibit such bistability. Yet the proximity in parameter space to the region defined by $\gamma_a + \alpha\gamma_p = 0$ (see Fig. 2), where the X and Y solutions interchange their stability, can play a key role in the degradation of the square-wave switching. We describe in Fig. 8 such degraded square-wave dynamics in the proximity of the parameter value $\gamma_a = -\alpha\gamma_p$. In this case, we also integrated the phase model as given by Eqs. (35) and (36) and reconstructed the intensity of the Y component as $I_y \sim |1 - e^{i\Phi}|^2$. In Fig. 8, the dynamics experiences a critical slowing down at the end of the second plateau where the LP-y component is off, and the escape from the weak saddle can be visualized as a noise-induced wandering in an almost flat landscape.

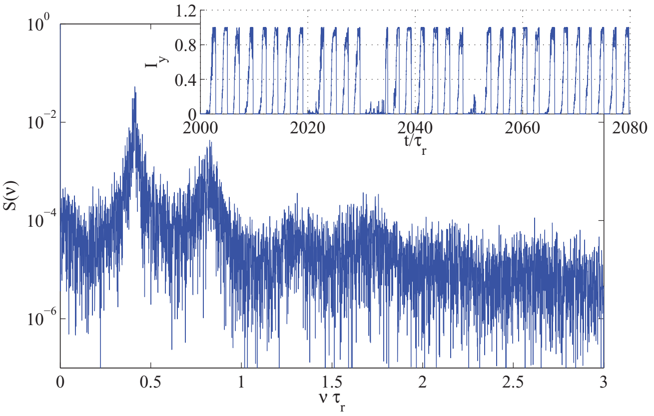

FIG. 8. (Color online) Square-wave switching dynamics in the presence of XPR. Time series (inset) and power spectrum for $\eta = 0$, $\gamma_a = -0.09$, $\beta = 0.25$, and $\tau_r = 500$. The signal is very irregular, and the period is noticeably slower than $2\tau_r$. The power spectrum does not show the signature of a square-wave signal with only odd harmonics.

However, a small amount of optical feedback has the effect of restabilizing the Y polarization and, incidentally, accelerating the escape from the saddle represented by emission into the LP-x mode. We describe in Fig. 9 such a regime and show that, even in the proximity of polarization switching, robust square-wave switching can be obtained for the proper choice of the feedback delay, i.e., $\tau_f \sim 2\tau_r$.

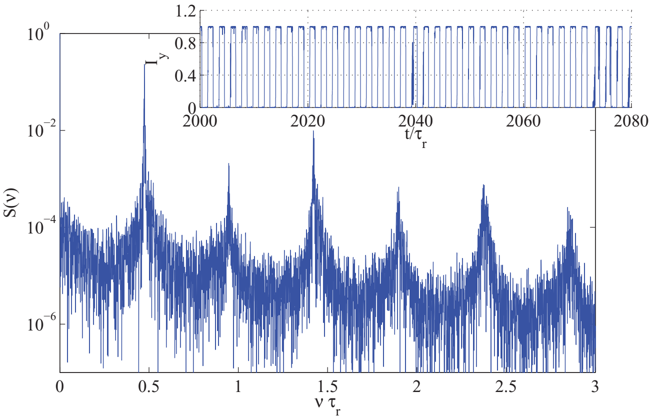

FIG. 9. (Color online) Square-wave switching dynamics in the presence of both XPR and PSF. Time series (inset) and power spectrum for $\eta = 0.05$, $\gamma_a = -0.09$, $\beta = 0.25$, $\tau_r = 500$, and $\tau_f = 1020$. The signal is much more regular, and the period is much closer than $2\tau_r$. The power spectrum shows the signature of a square-wave signal with only odd harmonics.

V. CONCLUSIONS

In this paper we have reduced the model describing the dynamics of the VCSEL with cross-polarized reinjection and/or with polarization-selective feedback to a model that consists of two phases: the orientation phase of the quasilinear polarization and the optical phase of the field. We have shown that the dynamics remains confined close to the equatorial plane of a Poincaré sphere with a given radius, which allowed us to decouple the relaxation oscillation for the total emitted power as well as the fluctuations in the ellipticity of the emitted light.

Such simplification, which is valid for bias currents far from the onset of laser emission, has allowed us to express analytically the modes in the presence of XPR and PSF and to shed some light on the complex modal structure given by this double-feedback configuration. We have also reinterpreted the square-wave switching dynamics reported in Refs. [19–21,31] as polarization orientation kinks. Close to the polarization switching the stability of both the LP-y and LP-x modes becomes marginal, which was shown to have a profound impact on the regularity of the antiphase square-wave switching induced by XPR. We have shown that, in the reduced phase model, the inclusion of optical feedback with a proper delay can also have the effect of regularizing the dynamics and that it can be used to mitigate the polarization degeneracy.

For future study we believe that a similar approach can be applied to the case of isotropic rotated feedback. Such an effect was shown to give antiphase polarization oscillations [16] up to frequencies of ∼10 GHz. Our method would yield a similar phase model, which would possibly allow us to study such polarization dynamics as a single dynamical equation. Also of great interest, our method can be extended readily to the case of polarized, and possibly detuned, optical injection.

ACKNOWLEDGMENTS

We acknowledge fruitful discussions with Salvador Balle and Bernd Krauskopf. J.J. acknowledges financial support from the Ramón y Cajal Fellowship, the CNRS for supporting a stay at the INLN where part of this work was developed, and financial support from project RANGER (TEC2012-38864-C03-01) and from the Direcció General de Recerca, Desenvolupament Tecnològic i Innovació de la Conselleria d'Innovació, Interior i Justí cia del Govern de les Illes Balears, cofunded by the European Union FEDER funds. M.M. and M.G. acknowledge funding from Région Provence-Alpes-Côte d'Azur for the "Projet Volet Générale 2011: Génération et Détection des Impulsions Ultra Rapides (GEDEPULSE)."

APPENDIX

The expression of $M_\pm$ and $F_\pm$ as used in Eqs. (5)–(10) reads

$$\begin{aligned}
M_+ &= \frac{\beta}{2} R_+^{\tau_r} \sin(\psi_+^{\tau_r} - \psi_+ - a) - \frac{\beta}{2} R_-^{\tau_r} \sin(\psi_-^{\tau_r} - \psi_+ - a)\\
&\quad + \frac{\eta}{2} R_+^{\tau_f} \cos(\psi_+^{\tau_f} - \psi_+ - \Omega)\\
&\quad - \frac{\eta}{2} R_-^{\tau_f} \cos(\psi_-^{\tau_f} - \psi_+ - \Omega),\\
M_- &= \frac{\beta}{2} R_+^{\tau_r} \sin(\psi_+^{\tau_r} - \psi_- - a) - \frac{\beta}{2} R_-^{\tau_r} \sin(\psi_-^{\tau_r} - \psi_- - a)\\
&\quad - \frac{\eta}{2} R_+^{\tau_f} \cos(\psi_+^{\tau_f} - \psi_- - \Omega)\\
&\quad + \frac{\eta}{2} R_-^{\tau_f} \cos(\psi_-^{\tau_f} - \psi_- - \Omega), \qquad \text{(A1)}\\
F_+ &= -\frac{\beta}{2} R_+^{\tau_r} \cos(\psi_+^{\tau_r} - \psi_+ - a) + \frac{\beta}{2} R_-^{\tau_r} \cos(\psi_-^{\tau_r} - \psi_+ - a)\\
&\quad + \frac{\eta}{2} R_+^{\tau_f} \sin(\psi_+^{\tau_f} - \psi_+ - \Omega)\\
&\quad - \frac{\eta}{2} R_-^{\tau_f} \sin(\psi_-^{\tau_f} - \psi_+ - \Omega),\\
F_- &= -\frac{\beta}{2} R_+^{\tau_r} \cos(\psi_+^{\tau_r} - \psi_- - a) + \frac{\beta}{2} R_-^{\tau_r} \cos(\psi_-^{\tau_r} - \psi_- - a)\\
&\quad - \frac{\eta}{2} R_+^{\tau_f} \sin(\psi_+^{\tau_f} - \psi_- - \Omega)\\
&\quad + \frac{\eta}{2} R_-^{\tau_f} \sin(\psi_-^{\tau_f} - \psi_- - \Omega).
\end{aligned}$$

The definitions of $\mathcal{A}, \mathcal{B}, \mathcal{H}_\pm, \mathcal{F}$, and $\mathcal{G}$ used in Eqs. (16)–(19) is

$$\mathcal{A} = \left[1 + \frac{\omega_r}{2}(D + d)\right]\cos^4\theta + \left[1 + \frac{\omega_r}{2}(D - d)\right]\sin^4\theta, \qquad \text{(A2)}$$

$$\mathcal{B} = \left(1 + \frac{\omega_r}{2} D\right)\sin(4\theta) + \omega_r d \sin(2\theta), \qquad \text{(A3)}$$

$$\mathcal{H}_+ = \left[1 + \frac{\omega_r}{2}(D + d)\right] I \cos^2\theta, \qquad \text{(A4)}$$

$$\mathcal{H}_- = \left[1 + \frac{\omega_r}{2}(D - d)\right] I \sin^2\theta, \qquad \text{(A5)}$$

$$\mathcal{F} = 2\frac{R_+ M_+ + R_- M_-}{P}, \qquad \text{(A6)}$$

$$\mathcal{G} = \frac{M_- R_+ - M_+ R_-}{I P}. \qquad \text{(A7)}$$

[1] J. Mulet, S. Balle, M. San Miguel, and C. R. Mirasso, in *IEEE 17th International Semiconductor Laser Conference* (IEEE, Piscataway, NJ, 2000), p. 101.

[2] J. Mulet and S. Balle, IEEE J. Quantum Electron. **38**, 291 (2002).

[3] J. Mulet and S. Balle, Phys. Rev. A **66**, 053802 (2002).

[4] S. Barland, J. R. Tredicce, M. Brambilla, L. A. Lugiato, S. Balle, M. Giudici, T. Maggipinto, L. Spinelli, G. Tissoni, T. Knodl, M. Miller, and R. Jager, Nature (London) **419**, 699 (2002).

[5] P. Genevet, S. Barland, M. Giudici, and J. R. Tredicce, Phys. Rev. Lett. **104**, 223902 (2010).

[6] A. K. J. van Doorn, M. P. van Exter, and J. P. Woerdman, Appl. Phys. Lett. **69**, 1041 (1996).

[7] G. Van der Sande, M. Peeters, I. Veretennicoff, J. Danckaert, G. Verschaffelt, and S. Balle, IEEE J. Quantum Electron. **42**, 898 (2006).

[8] M. P. van Exter, A. K. J. van Doorn, and J. P. Woerdman, Phys. Rev. A **56**, 845 (1997).

[9] K. D. Choquette, D. A. Richie, and R. E. Leibenguth, Appl. Phys. Lett. **64**, 2062 (1994).
[10] S. Balle, E. Tolkachova, M. San Miguel, J. R. Tredicce, J. Martín-Regalado, and A. Gahl, Opt. Lett. **24**, 1121 (1999).
[11] T. Ackemann and M. Sondermann, Appl. Phys. Lett. **78**, 3574 (2001).
[12] M. Sondermann, M. Weinkath, T. Ackemann, J. Mulet, and S. Balle, Phys. Rev. A **68**, 033822 (2003).
[13] K. Panajotov, M. Sciamanna, I. Gatare, M. Arteaga, and H. Thienpont, Adv. Opt. Technol. **2011**, 469627 (2011).
[14] M. Giudici, T. Ackemann, S. Barland, J. Tredicce, and S. Balle, J. Opt. Soc. Am. B **16**, 2114 (1999).
[15] F. Robert, P. Besnard, M. L. Chares, and G. M. Stephan, IEEE J. Quantum Electron. **33**, 2231 (1997).
[16] H. Li, A. Hohl, A. Gavrielides, H. Hou, and K. D. Choquette, Appl. Phys. Lett. **72**, 2355 (1998).
[17] J. Mulet, M. Giudici, J. Javaloyes, and S. Balle, Phys. Rev. A **76**, 043801 (2007).
[18] A. Gavrielides, T. Erneux, D. W. Sukow, G. Burner, T. McLachlan, J. Miller, and J. Amonette, Opt. Lett. **31**, 2006 (2006).
[19] J. Javaloyes, J. Mulet, and S. Balle, Phys. Rev. Lett. **97**, 163902 (2006).
[20] J. Mulet, J. Javaloyes, and S. Balle, IEEE J. Quantum Electron. **43**, 786 (2007).
[21] M. Marconi, J. Javaloyes, S. Barland, M. Giudici, and S. Balle, Phys. Rev. A **87**, 013827 (2013).
[22] K. L. Cooke and P. van den Driessche, J. Math. Biol. **35**, 240 (1996).
[23] S. Yongli, H. Maoan, and P. Yahong, Chaos Solitons Fractals **22**, 1139 (2004).
[24] G. Keqin, N. Silviu-Iulian, and C. Jie, J. Math. Anal. Appl. **311**, 231 (2005).
[25] A. R. Humphries, O. A. DeMasi, F. M. G. Magpantay, and F. Upham, Discrete Contin. Dyn. Syst., Ser. A **32**, 2701 (2012).
[26] B. Krauskopf and J. Sieber, Proc. R. Soc. A **470**, 20140348 (2014).
[27] P. Slowiński, B. Krauskopf, and S. Wieczorek, Proc. SPIE **7720**, 77200K (2010).
[28] P. Slowinski, B. Krauskopf, and S. M. Wieczorek, Discrete Contin. Dyn. Syst., Ser. B (to be published).
[29] S. Yanchuk and G. Giacomelli, Phys. Rev. Lett. **112**, 174103 (2014).
[30] T. Erneux, J. Danckaert, K. Panajotov, and I. Veretennicoff, Phys. Rev. A **59**, 4660 (1999).
[31] D. W. Sukow, T. Gilfillan, B. Pope, M. S. Torre, A. Gavrielides, and C. Masoller, Phys. Rev. A **86**, 033818 (2012).
[32] M. San Miguel, Q. Feng, and J. V. Moloney, Phys. Rev. A **52**, 1728 (1995).
[33] C. Henry, IEEE J. Quantum Electron. **18**, 259 (1982).
[34] J. Martín-Regalado, F. Prati, M. San Miguel, and N. B. Abraham, IEEE J. Quantum Electron. **33**, 765 (1997).
[35] D. Puzyrev, S. Yanchuk, A. Vladimirov, and S. Gurevich, SIAM J. Appl. Dyn. Syst. **13**, 986 (2014).
[36] K. Engelborghs, T. Luzyanina, and G. Samaey, DDE-BIFTOOL V. 2.00: A MATLAB package for bifurcation analysis of delay differential equations, Department of Computer Science, K. U. Leuven, Leuven, Belgium, 2001.
[37] H. Zhang, D. Y. Tang, L. M. Zhao, and X. Wu, Phys. Rev. B **80**, 052302 (2009).
[38] C. Lecaplain, P. Grelu, and S. Wabnitz, J. Opt. Soc. Am. B **30**, 211 (2013).